

Formation routes and structural details of the CaF_1 layer on $\text{Si}(111)$ from high-resolution noncontact atomic force microscopy data

Philipp Rahe*

Department of Physics and Astronomy, The University of Nottingham, University Park, Nottingham NG7 2RD, England, United Kingdom

Emily F. Smith

Nanoscale and Microscale Research Centre, The University of Nottingham, and School of Chemistry, The University of Nottingham, University Park, Nottingham NG7 2RD, England, United Kingdom

Joachim Wollschläger

Fachbereich Physik, Universität Osnabrück, Barbarastrasse 7, 49076 Osnabrück, Germany

Philip J. Moriarty

Department of Physics and Astronomy, The University of Nottingham, University Park, Nottingham NG7 2RD, England, United Kingdom



(Received 17 November 2017; revised manuscript received 22 January 2018; published 15 March 2018)

We investigate the $\text{CaF}_1/\text{Si}(111)$ interface using a combination of high-resolution scanning tunneling and noncontact atomic force microscopy operated at cryogenic temperature as well as x-ray photoelectron spectroscopy. Submonolayer CaF_1 films grown at substrate temperatures between 550 and 600 °C on $\text{Si}(111)$ surfaces reveal the existence of two island types that are distinguished by their edge topology, nucleation position, measured height, and inner defect structure. Our data suggest a growth model where the two island types are the result of two reaction pathways during CaF_1 interface formation. A key difference between these two pathways is identified to arise from the excess species during the growth process, which can be either fluorine or silicon. Structural details as a result of this difference are identified by means of high-resolution noncontact atomic force microscopy and add insights into the growth mode of this heteroepitaxial insulator-on-semiconductor system.

DOI: [10.1103/PhysRevB.97.125418](https://doi.org/10.1103/PhysRevB.97.125418)

I. INTRODUCTION

Thin insulating films have been exploited very successfully as a decoupling layer to isolate an adsorbed molecule from an underlying substrate, enabling an analysis of the molecular adsorbate in a state free from the distorting effects of chemisorption. As a key prototype system, NaCl films on (111) surfaces of metals such as, e.g., Cu or Au, have been explored [1], and in an early study the frontier orbitals of molecular adsorbates on NaCl bilayers have been found to closely resemble the orbital structure of the molecule in the gas phase [2]. Furthermore, charge stability of single adatoms [3,4] and molecules [5,6] has been realized using NaCl films on Cu(111), and very recently a strong hysteresis opening of a single-molecule magnet adsorbed on MgO thin films has been observed at low temperature [7]. Nonetheless, charge leakage through thin insulating layers is still a major challenge for molecular device functionality [8].

Due to the small lattice mismatch of 0.6% at room temperature between silicon and the ionic material CaF_2 , the growth of CaF_2 particularly on (111) surfaces of silicon has early been identified as a promising system for insulator-semiconductor devices, and has especially been studied in

the context of resonant tunneling diodes [9–11]. Besides this application-oriented relevance, CaF_2 on $\text{Si}(111)$ is of fundamental interest in understanding the growth and properties of heteroepitaxial systems and has consequently been intensively studied. Recently, also the growth of NaCl [12,13] (lattice mismatch with Si about 4%) and KCl [14,15] (lattice mismatch with Si more than 10%) thin films on surfaces of silicon has been investigated. A short review summarizing the extensive characteristics of CaF_2 deposited on $\text{Si}(111)$ will be given in Sec. II. Especially, when deposited on silicon surfaces held at elevated temperatures, CaF_2 dissociates to form a CaF_1 layer in an interface reaction with silicon. Finally, due to the large CaF_2 band gap, the homogeneous growth modes of CaF_2 on silicon, and the recent success of molecular assembly on bulk CaF_2 surfaces [16–19], the $\text{CaF}_2/\text{Si}(111)$ system has the potential to act as an insulator-on-semiconductor complement to the insulator-on-metal systems currently used for studying molecular decoupling.

Here, we investigate the atomic structure, morphology, and defect formation for a submonolayer CaF_1 interface film grown at substrate temperatures between about 550 and 600 °C by using a combination of high-resolution scanning tunneling microscopy (STM) and frequency modulated non-contact atomic force microscopy (NC-AFM) with a tuning fork sensor in qPlus configuration [20] and operated at cryogenic temperatures. The high-resolution NC-AFM data enable the investigation of atomic-scale details of the CaF_1/Si system

*Present address: Fachbereich Physik, Universität Osnabrück, Barbarastrasse 7, 49076 Osnabrück, Germany; prahe@uni-osnabrueck.de

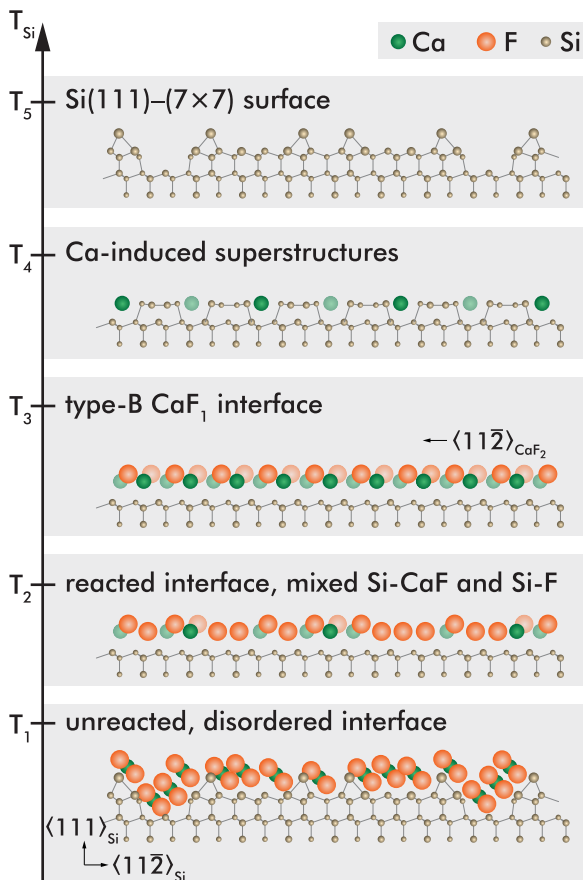


FIG. 1. Models proposed in literature for the interface structures after (sub-)monolayer deposition of CaF_2 on the $\text{Si}(111)-(7 \times 7)$ surface. The different models are arranged by the substrate temperature T_{Si} used during film growth or in a second annealing step after deposition. Due to the complex dependence on other preparation parameters, structures including a mix of the presented phases are not uncommon. Directions referring to the Si (CaF_2) lattice are named $\langle hkl \rangle_{\text{Si}}$ ($\langle hkl \rangle_{\text{CaF}_2}$).

that are not available from STM experiments. Additionally, scanning probe microscopy (SPM) methods in general avoid sample modification that has been observed for this system upon electron irradiation [21]. The SPM data are complemented by x-ray photoelectron spectroscopy (XPS) to measure the film stoichiometry. In particular, high-resolution cryogenic NC-AFM data allow us to clarify three structural aspects of the $\text{CaF}_1/\text{Si}(111)$ interface structure that remained unclear so far, namely, the step edge termination as well as point and line defect structures. Our data suggest a growth model that involves two reaction pathways.

II. PROPERTIES OF THE $\text{CaF}_2/\text{Si}(111)$ SYSTEM

The complex interface structure formation and multilayer growth modes of $\text{CaF}_2/\text{Si}(111)$ have been summarized in recent reviews [22–24]; an overview of the different models observed for the interface structure after CaF_2 deposition is shown in Fig. 1.

When deposited with the sample held at room temperature (T_1 in Fig. 1), CaF_2 has been observed to physisorb on the

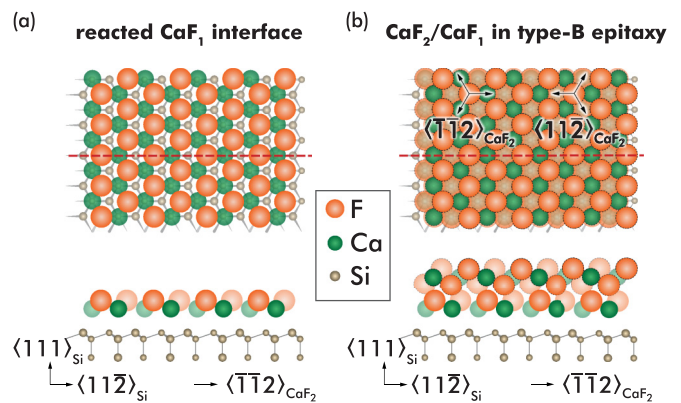


FIG. 2. Geometric structures of (a) CaF_1 and (b) $\text{CaF}_2/\text{CaF}_1$ on $\text{Si}(111)$ surfaces. Following Ref. [22], the Ca atoms are depicted at the T_4 site on the $\text{Si}(111)-(1 \times 1)$ surface. Equivalent directions of CaF_2 are included in panel (b).

$\text{Si}(111)-(7 \times 7)$ reconstructed surface in a rather disordered fashion after direct deposition [25]; core level spectroscopy does not give evidence for CaF_2 dissociation [26] and the (7×7) reconstruction is not removed [27]. Although the interface is rather disordered at low substrate temperatures T_{Si} during deposition, addition of further CaF_2 at substrate temperatures T_{Si} up to about 400°C leads to multilayer films grown in type-A epitaxy [27–30]. In this epitaxial mode, the orientation of the CaF_2 film is identical to the underlying $\text{Si}(111)$ surface lattice; especially, the equivalent $\langle 11\bar{2} \rangle_{\text{Si}}$ directions of the silicon surface lattice are identical to the equivalent $\langle 11\bar{2} \rangle_{\text{CaF}_2}$ directions of the adsorbed CaF_2 film. To distinguish these two coordinate systems, we use herein the nomenclature $\langle hkl \rangle_{\text{CaF}_2}$ and $\langle hkl \rangle_{\text{Si}}$ when referring to the equivalent directions of the $\text{CaF}_2(111)$ and $\text{Si}(111)$ surface lattice, respectively. Due to the $p3m1$ planar space-group symmetry of the $\text{Si}(111)$ and $\text{CaF}_2(111)$ surfaces (including the infinite half space underneath), the three equivalent $\langle 11\bar{2} \rangle$ surface directions are $[\bar{1}\bar{1}2]$, $[\bar{1}2\bar{1}]$, and $[2\bar{1}\bar{1}]$, with the three equivalent $\langle 11\bar{2} \rangle$ surface directions $[11\bar{2}]$, $[1\bar{2}1]$, and $[21\bar{1}]$ pointing opposite [see also Fig. 2(b)].

However, when CaF_2 is either deposited at higher substrate temperatures T_{Si} , or if the CaF_2 -covered $\text{Si}(111)$ surface is annealed after deposition, substantial structural and chemical transitions occur [22,26,26,31–33] (see T_2 in Fig. 1). First, type-A films below a thickness of about 5 triple layers have been found to undergo a transition to type-B epitaxy at higher temperatures [27,29,30,34]; the in-plane crystallographic axes of the CaF_2 film are rotated by 180° relative to the $\text{Si}(111)$ substrate in this type-B epitaxial mode [35]. In particular, the equivalent $\langle 11\bar{2} \rangle_{\text{CaF}_2}$ directions of the CaF_2 lattice and the equivalent $\langle 11\bar{2} \rangle_{\text{Si}}$ directions of the silicon substrate are antiparallel in type-B epitaxy as sketched in Fig. 2(a).

Second, the switch in the epitaxial growth mode is accompanied by a change in the stoichiometry of the CaF_x interface layer. While CaF_2 remains intact when deposited on samples held at room temperature [26], Tromp and Reuter identified a F:Ca ratio of about 1:1 after deposition at $T_{\text{Si}} \sim 770^\circ\text{C}$, forming a film with a coverage of one Ca and one F atom per (1×1) unit cell [32] (see T_3 in Fig. 1). This CaF_1 stoichiometry

has also been found by Olmstead [22] and Olmstead and Bringans [26] for growth temperatures above $\sim 550^\circ\text{C}$ and was confirmed in further studies [31,33]. The CaF_1 interface layer is formed before CaF_2 multilayers can be grown in type-B epitaxy [see also Fig. 2(b)].

Third, upon further increasing the substrate temperature T_{Si} , the F:Ca ratio decreases due to further dissociation of CaF_1 and the desorption of fluorine. With the decreasing F:Ca ratio, a series of surface reconstructions has been observed for the intermediate F-depleted film above 650°C [36,37], finally evolving into an apparent 3×1 reconstruction where fluorine is absent [38] (see T_4 in Fig. 1). This apparent reconstruction has also been observed for pure Ca deposition on Si(111) surfaces [39], and has been identified to be actually formed by a mixture of 3×2 and $c(6 \times 2)$ reconstructions [40]. At even higher temperatures T_{Si} , all Ca eventually leaves the surface; this complete reevaporation of the CaF_2 film restores the Si(111)-(7 \times 7) surface [36] (see T_5 in Fig. 1).

At sub- and few-monolayer coverages (and at a sample temperature of $T_{\text{Si}} = 500^\circ\text{C}$), Si $2p$ core-level shifts of 0.4 eV to lower binding energy and of 0.8 eV to higher binding energy have been observed in XPS experiments [31,33,36], which were attributed to Si-Ca and Si-F bonds, respectively. A corresponding shift of the Ca $2p$ spin-orbit split doublet of about 2.7 eV to lower binding energy has been measured [33,41,42], while shifts of the F $1s$ component may be compensated by other effects [33] and are, thus, not visible. However, despite the observation of Si-F bonds [33,38,43–45], they are attributed to residual fluorine after heating below the optimal growth temperature [38]. Instead, if the interface is grown using optimal growth parameters, exactly half of the fluorine is desorbed, resulting in an ordered CaF_1 interface layer with strong Si-Ca bonds between the silicon surface and the CaF_1 molecules [38] [see also Fig. 2(a)] and an absent Si-F component.

XRD studies showed the formation of interfaces with basically two different distances between the silicon atoms of the surface and the calcium atoms of the film. The shorter distance was attributed to clean interfaces, while the longer distance seems to be formed due to an additional contaminating monolayer at the interface [29,30,46–51]. An irreversible change in the silicon- CaF_1 interface distance from the short to the long interface has been attributed to modifications after air exposure or aging of the film [22,30]. Therefore, extremely clean conditions, such as growth and characterization under ultrahigh vacuum, have to be used to ensure a well-defined interface structure [22,25].

The morphology, atomic structure, and composition of CaF_x/Si films have also been investigated by SPM, mainly using STM as well as AFM operated in contact, friction, or frequency-modulated noncontact mode. The first STM study on this system has been performed by Avouris and Wolkow, who imaged submonolayer coverages and discussed the STM imaging mechanism including the band structure of the $\text{CaF}_2/\text{CaF}_1/\text{Si}(111)$ system [52]. Later, by using STM and scanning tunneling spectroscopy (STS), differences in the imaging of the CaF_1 and CaF_2 areas have been identified by other groups [53,54]. Nakayama *et al.* [55,56] investigated defect structures within the CaF_1 interface layer grown on Si(111) and suggested that the depressions imaged in STM are formed by clusters of excess Si atoms. Further studies focused

on the morphology of submonolayer and multilayer films, where different growth modes and morphologies from varying the substrate temperature during deposition or measurement could directly be imaged [34,37,57–59].

A small number of studies have been performed using atomic force microscopy, most of them in contact mode [34,60–62]. Recently, Klust *et al.* presented material-dependent [63] as well as atomically resolved [64] data using *in vacuo* frequency-modulated NC-AFM, identifying the CaF_1 and CaF_2 areas and revealing the atomic lattice with similar contrast as has been observed before on (111) surfaces of CaF_2 crystals [65,66].

III. METHODS

Sample preparation and SPM experiments were performed under ultra-high-vacuum conditions with a base pressure better than 1×10^{-9} mbar during sample preparation and transfer, and better than 5×10^{-11} mbar during SPM measurements. Highly B-doped ($0.02 \Omega \text{ cm}$) p-type Si samples (Institute of Electronic Materials Technology, Warsaw, Poland) with small miscut were prepared by usual flash cycles after an initial anneal whereby the (7 \times 7) reconstruction is formed. The Si crystal orientation is determined by identifying the equivalent $\langle 11\bar{2} \rangle_{\text{Si}}$ directions of the silicon lattice from filled-state STM images, where the apparent height difference of the faulted and unfaulted half is resolved [67]. The single-crystal CaF_2 material (99.9% from AlfaAesar, UK) was deposited using an EFM3T e-beam sublimator (Focus GmbH, Germany) operated without ion filtering. The Si sample was directly heated during the deposition; the substrate temperatures stated herein were measured using an optical pyrometer (model MM1M from Raytek, Berlin, Germany). Very low deposition rates for the CaF_2 deposition were used.

STM and NC-AFM experiments were performed with an LT qPlus instrument (Scienta Omicron GmbH, Taunusstein, Germany) operated at 77 K with a MATRIX control system. The bias voltage U_{bias} is given with respect to the sample voltage, i.e., positive voltages refer to probing unoccupied states. qPlus sensors fabricated by the supplier as well as home-build sensors, both equipped with chemically etched W tips, are used without further preparation besides treatment on Si(111) surfaces. All NC-AFM measurements were carried out at a bias of 0 V to avoid crosstalk between the measurement channels [68]. The setup is complemented by an atom-tracking system to compensate for thermal drift [69] and all data were analyzed using GWYDDION [70].

XPS experiments were performed in a separate vacuum system at a base pressure better than 7×10^{-9} mbar. After sample preparation and SPM experiments, samples were transferred under vacuum using a small transfer chamber. They were analyzed using the Kratos AXIS ULTRA with a monochromated Al K_α x-ray source (1486.6 eV) operated at 10 mA emission current and 12 kV anode potential (120 W). The instrument was used in fixed analyzer transmission mode, which has constant energy resolution along the energy scale. The magnetic immersion lens system allows for the area of analysis to be defined by apertures; a “slot” aperture of $300 \times 700 \mu\text{m}$ for wide/survey scans and high-resolution scans was set. The takeoff angle for the photoelectron analyzer is 90° and has an

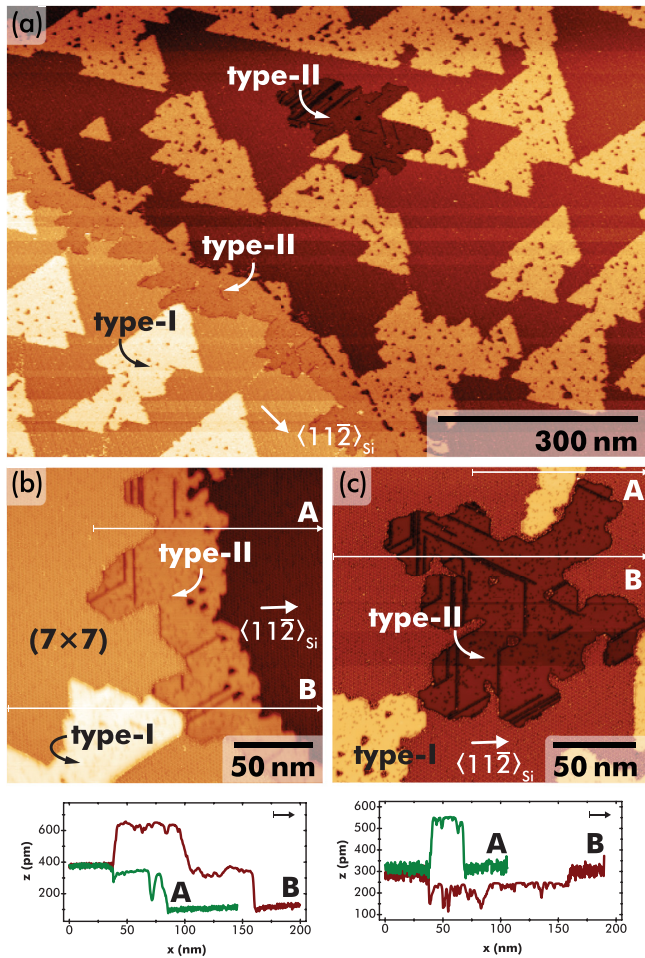


FIG. 3. Two island types identified at submonolayer coverages of CaF_1 on $\text{Si}(111)$ marked by “type-I” and “type-II.” Islands are surrounded by bare (7×7) regions as indicated. Imaging parameters: (a) $U_{\text{bias}} = -3.0$ V, 220 pA and (b,c) $U_{\text{bias}} = -3.0$ V, 50 pA. Line profiles extracted at positions marked in panels (b) and (c).

angular acceptance of 9° for hybrid lens mode. Wide survey scans (not shown) and high-resolution scans were acquired on each sample. The peak areas in the data can be used to calculate the elemental atomic percent using Kratos relative sensitivity factors (RSFs). High-resolution scans were run for 5 min each with pass energy 20 eV and step size of 0.1 eV for F 1s and Ca 2p energy regions. We measured at three separate positions on each sample and used the average of one recorded spectrum for further analysis from each position. Data processing was carried out using CASAXPS (version 2.3.17 dev 6.6) with Kratos RSFs to determine atomic percent values from the peak areas. Each peak area is calculated as the integrated intensity after subtracting a linear background from the respective peak regions.

IV. RESULTS

We investigate samples with submonolayer depositions of CaF_2 on pristine $\text{Si}(111)$ - (7×7) surfaces held at temperatures T_{Si} of about 550 to 600 $^\circ\text{C}$ during deposition; an exemplary large-scale STM image is shown in Fig. 3(a). At these prepara-

tion parameters, the film grows in type-B epitaxy in form of the CaF_1 interface layer, where half of the fluorine is desorbed after dissociation of CaF_2 . We will measure the F:Ca stoichiometry by XPS in Sec. V.

Topography data acquired in constant-current feedback reveal two characteristic island structures: hummocklike islands [marked “type-I” in Figs. 3(a) and 3(b)] as well as islands close-by step edges [marked “type-II” in Fig. 3(b)] or located as embedded islands on bare terraces [71] of the $\text{Si}(111)$ surface, but imaged lower than the surrounding (7×7) surface [marked “type-II” in Fig. 3(c); see also line profiles below the STM images]. Although mixed terrace (type-I islands) and step (partly type-II islands) nucleation has been related before to the substrate temperature during growth as well as the terrace width [72,73], subtle differences regarding the structures of these two islands become evident from our data.

While type-I islands are associated with largely straight-appearing step edges oriented along three principal directions (see detailed discussion below), type-II islands have smoother, i.e., less “angular,” edges and frequently exhibit inner line defects. Additionally, and in agreement with earlier STM studies [55,56], all islands contain small black depressions.

Type-I islands are imaged with heights around 2–4 \AA , while type-II islands are imaged lower by less than 1 \AA relative to the surrounding higher Si step [see line profiles in Figs. 3(b) and 3(c)]. Although height measurements in STM are generally dependent on the applied sample bias, we are confident from NC-AFM data that the chosen imaging parameters correctly reflect the relative height order. This observation is in agreement with STS measurements on the CaF_1 interface layer, where a peak 0.4 eV below the Fermi level was found to lead to high conductance through the insulating material [54]. The height of the calcium (top fluorine) atoms above the topmost silicon plane has been determined to be about 2.6 \AA (3.4 \AA) using the x-ray standing-wave technique [45].

A. Edges of type-I islands

High-resolution STM and NC-AFM data from two isolated type-I islands are shown in Fig. 4. We can identify two step edge types of the island, namely, straight short [marked by “A” in Fig. 4(a)] and “fuzzy” long [marked by “B” in Fig. 4(a)] edges. The apparent orientation of these two step edges is along two nonequivalent lattice directions as determined from the silicon crystal orientation and the type-B epitaxial growth mode: the $\langle \bar{1}\bar{1}2 \rangle_{\text{CaF}_2}$ ($\langle 11\bar{2} \rangle_{\text{CaF}_2}$) directions are perpendicular to the “A” (“B”) edge. These two island edge types have been identified before by Nakayama and Aono [56] using STM, where it was suggested that the difference in their morphology is caused by the different growth fronts that lead to different densities of free Si atoms during etching the (7×7) reconstruction. As the STM contrast is limited at the step edges themselves, we use high-resolution NC-AFM imaging to investigate the atomic structure of these two CaF_1 interface layer island edges. From the constant- Δf NC-AFM data in Fig. 4(b) we reveal small peaks protruding from the fuzzy edge type; the outlines of these peaks are strongly blurred yet visible within the STM data. Interestingly, the peak edges are again oriented parallel to the island edges of type A, namely, with the $\langle \bar{1}\bar{1}2 \rangle_{\text{CaF}_2}$ directions perpendicular to the edges. Consequently, our data suggest that

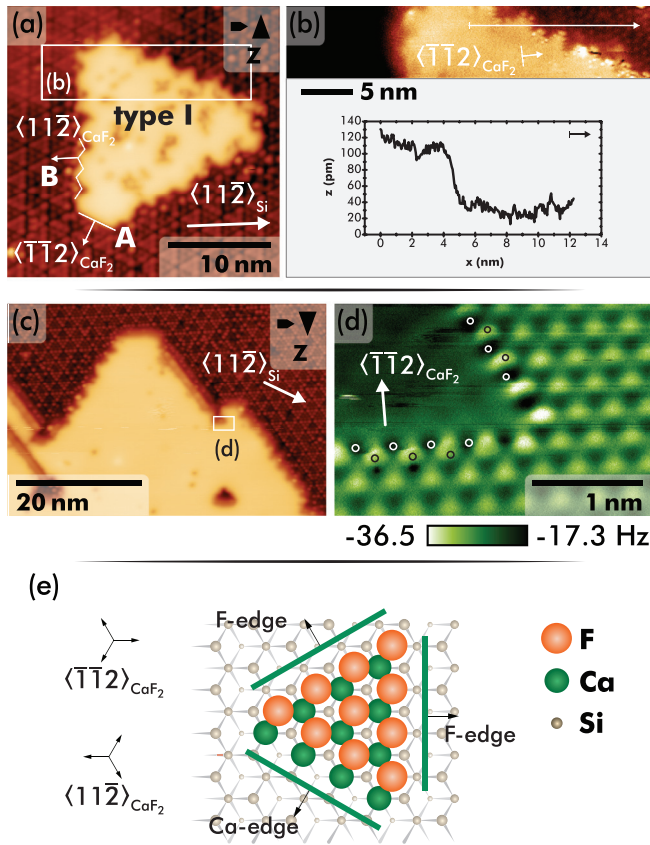


FIG. 4. (a), (c) STM and (b), (d) NC-AFM images of type-I CaF_1 island edges showing (a), (c) the island outline and (b), (d) details of island edges. (e) Model of a CaF_1 island with edges having normal vectors along $\langle \bar{1}\bar{1}2 \rangle_{\text{CaF}_2}$ directions. The three equivalent surface directions in the (111) plane are drawn to the left. Imaging parameters: (a) STM in constant-current feedback, $U_{\text{bias}} = -3$ V, $I_{\text{set-point}} = 50$ pA. (b) NC-AFM in constant- Δf feedback at $U_{\text{bias}} = 0$ V, $\Delta f_{\text{set-point}} = -17.6$ Hz. (c) STM in constant-current feedback, -3 V, 10 pA. (d) Constant-height NC-AFM imaging at 0 V.

edges with the $\langle \bar{1}\bar{1}2 \rangle_{\text{CaF}_2}$ directions as normal vectors are the stable step edge termination.

In a next step, the atomic structure of $\langle \bar{1}\bar{1}2 \rangle_{\text{CaF}_2}$ step edges is investigated. Figure 4(d) is a constant-height scan acquired in NC-AFM mode at the acute corner site marked in the STM image in panel (c). The atomic lattice of the CaF_1 interface layer is clearly imaged and thus the atomic edge structure of the two (crystallographically identical) edges can be studied in some detail. The edge is terminated by a row of atoms with a $\langle \bar{1}\bar{1}2 \rangle_{\text{CaF}_2}$ direction oriented perpendicular to the edge. Due to the type-B epitaxy, with knowledge of the $\langle 11\bar{2} \rangle_{\text{Si}}$ directions from imaging the (7×7) reconstruction, and from earlier results concluding that Ca is located at the T_4 site [22], we can propose two possibilities for the step termination in Fig. 4(e): the step is expected to be terminated either by protruding F atoms (denoted “F-edge”) or by Ca atoms located in front of the edge (denoted “Ca-edge”). As the NC-AFM image reveals a zig-zag arrangement for the two features closest to the edge [circles are included in Fig. 4(d) as a guide to the eye], our data suggest that the fluorine-terminated edge is the likely structure.

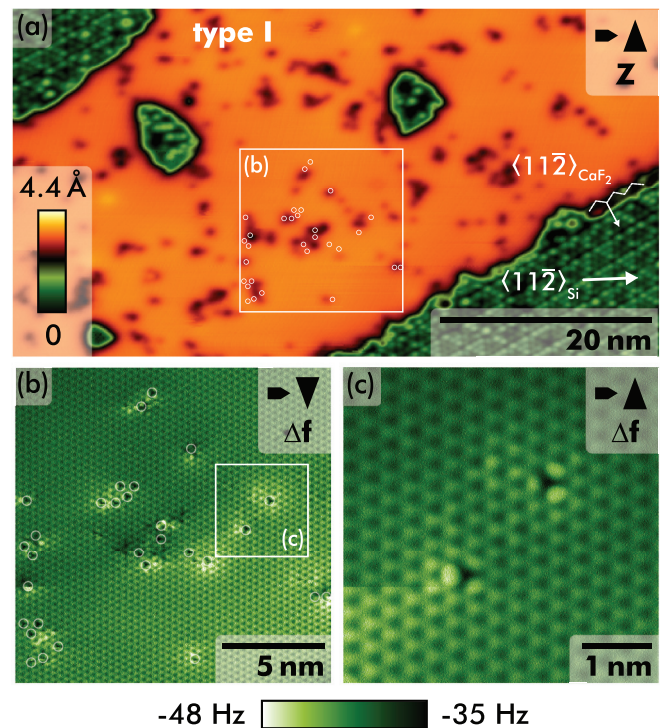


FIG. 5. (a) STM and (b), (c) constant-height NC-AFM images of type-I CaF_1 islands with defects. The positions of the detailed scans in panels (b) and (c) are marked in panels (a) and (b), respectively. STM imaging parameters: $U_{\text{bias}} = -3$ V, 50 pA. NC-AFM imaging at 0 V.

Thus, the CaF_1 interface layer islands seem to exclusively form fluorine-terminated $\langle \bar{1}\bar{1}2 \rangle_{\text{CaF}_2}$ oriented step edges. Our data especially show that the peaks revealed at type-B edges are also formed by small sections of edges with $\langle \bar{1}\bar{1}2 \rangle_{\text{CaF}_2}$ orientation—and not by edges with the apparent $\langle 11\bar{2} \rangle_{\text{CaF}_2}$ orientation. It is interesting to note that $\langle \bar{1}\bar{1}2 \rangle_{\text{CaF}_2}$ edges on bulk CaF_2 are polar [74] and different structure models have been proposed [74–77]. In the case of the CaF_1 interface layer, the removal of the lower F atoms might, in contrast, stabilize this edge type.

B. Defect structures

Next, we focus on the defect structures within the islands. Figure 5 presents STM [panel (a)] and constant-height NC-AFM [panels (b) and (c)] data acquired on a type-I island. The STM image reveals the common structure of fuzzy type-B edges with the apparent edge normal vector along the $\langle 11\bar{2} \rangle_{\text{CaF}_2}$ directions (see discussion before) as well as dark spots within the island. Similar defect structures have been observed before [55,56], and have been explained to be formed by excess Si atoms.

Here, we additionally apply high-resolution NC-AFM to resolve the atomic structure of type-I islands with the data reproduced in Figs. 5(b) and 5(c). Both images are frequency-shift Δf images acquired in constant-height mode. Besides clearly resolving the atomic lattice, where imaging triangular features of atomic size on bulk CaF_2 surfaces has been explained before by the presence of a positive potential tip [65], we can identify single point defects.

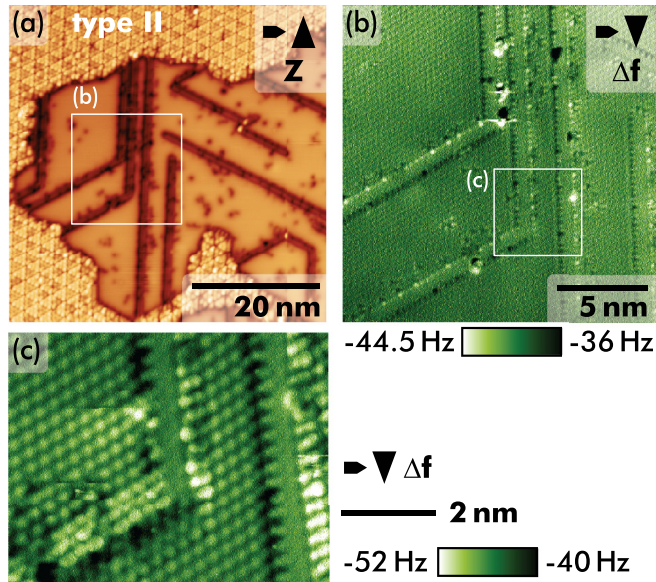


FIG. 6. (a) STM and (b), (c) constant-height NC-AFM images of type-II islands with rowlike defect structures. The positions of the detailed scans in panels (b) and (c) are marked in panels (a) and (b), respectively. STM imaging parameters: $U_{\text{bias}} = -3$ V, 50 pA. NC-AFM imaging at 0 V.

The positions of the defects resolved in Fig. 5(b) (marked with circles) are superimposed on the STM data in panel (a) at the image position. Interestingly, most of the defect positions match the dark depressions imaged in STM mode. These dark depressions in STM topography data result from a reduced conductivity at the specific positions and usually point to the presence of dopant atoms or vacancies. In the NC-AFM data, the dominant defect species is identified as a black depression of atomic size surrounded by a three-lobed structure [see high-resolution image in Fig. 5(c)]. The different orientations of the three lobes for two different defects exclude a tip artifact in imaging these lobes, but rather suggest a defective site with partial relaxation of the surrounding atoms. Based on STM experiments, Nakayama *et al.* [55,56] have speculated that the defects are caused by excess Si atoms that remain in the CaF_1 interface structure after etching the (7×7) reconstruction. Despite the comparable large appearance of the defects in STM, our NC-AFM data clearly do not support the presence of a large number of excess Si atoms within the single defects. However, the existence of point defects is in agreement with an increased friction on the interface layer as measured in lateral friction force microscopy experiments [62].

Another frequently observed feature—especially within islands of type-II—is a straight row running along one of the $\langle \bar{1}10 \rangle_{\text{Si}}$ directions. Figure 6 shows these rows on a type-II island in both STM [panel (a)] and constant-height NC-AFM [panels (b) and (c)] mode. Additionally to these rows, the data show also the single-point defects that have been discussed before.

The atomic resolution NC-AFM data acquired on type-II islands reveal a (1×1) lattice structure as observed for type-I islands; we can therefore exclude that this island type is already formed by one of the high-temperature reconstructions [36]. Consequently, the imaged rows are different from row

structures due to reconstructions that have been observed with STM on samples prepared at higher temperatures before [37,52,57,59,78]. In fact, we can induce high-temperature reconstructions by annealing the sample above 600°C (data not shown).

Another explanation has been put forward by Kametani *et al.* [79]. Using positive sample bias STM data, they also revealed rows running along the $\langle \bar{1}10 \rangle_{\text{Si}}$ directions for a film prepared at a temperature of 630°C . Within their STM data, the rows have been imaged as protrusions with a height of the order of the (111) layer separation of CaF_2 . Consequently, they suggested a second-layer model, where rows of CaF_2 already grow on the CaF_1 interface layer before the interface layer is closed.

During our experiments we found that the imaged height of these rows in STM can be dependent on the tip state (possibly by ion exchange [80] with the CaF_1 film), and the sample bias. In one particular case (data not shown), a tip change modified the imaged height from $+1.0$ to -0.5 Å relative to the surrounding areas, thus even changing a protrusion to a depression.

Additionally, constant-height NC-AFM data [see Figs. 6(b) and 6(c)] reveal a void regime within the row structure: while the (1×1) structure is clearly imaged aside the rows, no strong interaction is measured within the row structure. It is known that the contrast formation for NC-AFM highly depends on the sample system and tip characteristics [81]; however, based on the recent understanding of high-resolution studies using functionalized tips, Pauli repulsion will eventually be measured in the presence of atoms [82,83]. Therefore, our data do not support a model of additional CaF_2 rows adsorbed on top of the CaF_1 interface layer, but rather suggest a lower-lying surface. Based on the analysis of the interface reaction in Sec. V, our data suggest that the rows are formed by excess silicon material.

C. XPS results

To verify the presence of a reacted interface layer including the desorption of half of the fluorine atoms, we attempted to quantify the stoichiometry of the surface using XPS measurements of the Ca $2p$ and F $1s$ core levels. To account for thin-film effects when investigating submonolayer CaF_x structures on Si(111), we furthermore prepared a control sample where CaF_2 was deposited on Si(111)- (7×7) at room temperature.

The samples were transferred under vacuum to the XPS system to minimize contamination [22,30]. Representative spectra acquired on the sample imaged in STM [Fig. 3(a)] are presented in Fig. 7, where the Ca $2p$ spin-orbit split doublet [panel (a)] and the F $1s$ single peak [panel (b)] are clearly resolved. Spectra have been aligned by shifting the Si $2p_{3/2}$ component to 99.3 eV. The measured binding energy of 348.5 eV for the Ca $2p_{3/2}$ components resembles the expected core level shift after the Si-Ca interface formation [41,42].

The Ca $2p$ and F $1s$ peaks are at different kinetic energies, thus the sampling depth is slightly different. To account for this effect during the following quantification, we deposited a thin film of CaF_2 with the substrate held at room temperature as a reference sample for XPS. CaF_2 films deposited at room temperature are disordered, but are of known stoichiometry with a F:Ca ratio of 2:1 (in the following denoted as 2) as the

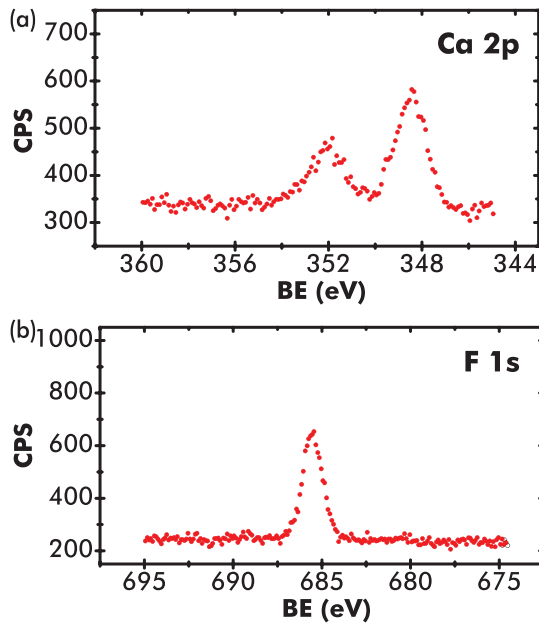


FIG. 7. High-resolution XPS scans of the (a) Ca $2p$ and (b) F $1s$ peak regions for the sample shown in Fig. 3(a) and acquired at one position. The CaF_1 interface layer was prepared using substrate temperatures between 550 and 600 °C during deposition.

CaF_2 dissociation (or formation of CaF_1) is avoided [22]. The relative peak intensity from this sample was then used to adjust the measured stoichiometry of the CaF_1 sample. This strategy allows us to determine a F:Ca ratio of 1.1 ± 0.2 for the sample imaged in Fig. 3(a). The fluorine signal did not significantly decrease in consecutive scans over several hours, i.e., we do not see evidence for fluorine removal. This is in agreement with earlier findings where the stability of fluorine in the interface layer has been found to be much higher than in the bulk or in bulk films during electron exposure [21].

V. DISCUSSION

In order to investigate the difference between the island types, it is helpful to discuss the different steps in the Si etching and CaF_1 interface formation process. To begin with, we can exclude the possibility that the islands contain significantly more fluorine than present within a CaF_1 interface layer due to the quantification derived from our XPS data. Thus, the following analysis assumes the existence of an interface layer with CaF_1 stoichiometry. With this result, the island types identified here are different from the two island types on a multilayer sample observed by Wang *et al.* [61] and, additionally, we can exclude high-temperature interface reconstructions due to an F:Ca ratio falling significantly below 1 [37]. Furthermore, as all experiments were performed under ultra-high-vacuum conditions, we are confident that we do not investigate a contaminated surface after air exposure [22,30]. Last, for the following model we exclude the possibility of pure Si desorption during CaF_2 deposition due to the low substrate temperatures compared to the Si desorption temperature.

The Si surface has to reorganize substantially when the interface reaction removes the Si (7×7) reconstruction to form

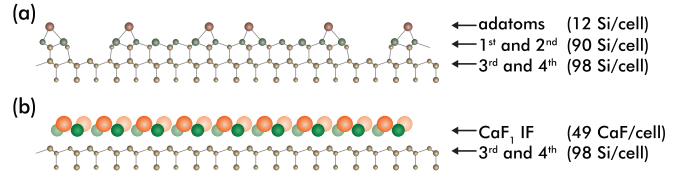


FIG. 8. Structures of the (a) dimer-adatom-stacking fault (DAS) model of the Si(111)- (7×7) reconstruction [84] and (b) reacted $\text{CaF}_1/\text{Si}(111) - (1 \times 1)$ interface.

the $\text{CaF}_1/\text{Si}(111) - (1 \times 1)$ interface. The 12 adatoms within the Si (7×7) unit cell are located above 90 atoms in the first and second reconstructed layer [84] [see also Fig. 8(a)]. From the third layer downwards, the unreconstructed bulk structure is maintained; 98 silicon atoms are present per (7×7) unit cell in each layer pair.

The necessity for the 102 Si atoms in the top layers to redistribute has been identified before to play a critical role in the formation of superstructures on silicon. For example, the (7×7) to (3×1) transformation induced by the deposition of Na on a heated Si(111)- (7×7) surface causes the formation of a two-level system of Na-reconstructed islands on Na-reconstructed terraces due to excess silicon atoms [85]. For the deposition of Ca on Si(111)- (7×7) surfaces, a similar two-level system has been observed after room-temperature Ca deposition followed by annealing, while deposition onto heated substrates has led to step bunching [40]. For the case of CaF_2 on Si(111), Nakayama *et al.* [55] identified before a total of four excess silicon atoms in the first layer during the interface formation or as a result of filling the cornerholes, and discussed their presence within the resulting interface. However, and also as an important difference to the processes revealed for Ca or for Na restructuring silicon surfaces [40,85], the known desorption of SiF_x species during the etching step [22,61] offers a route to remove excess silicon and, consequently, cannot be ignored in the species quantification.

Based on our SPM data we propose the presence of two reaction routes, each leading to one of the two island types. The height of type-I islands measured in both STM filled-state and NC-AFM Δf -feedback imaging are in agreement with islands protruding from the surface, thus the etching process likely removes or rearranges the adatoms of the (7×7) reconstruction to form the Si(111) - (1×1) termination. In contrast, type-II islands are imaged lower, thus our data suggest a CaF_1 interface formation after etching the silicon down to and including the second Si layer [see also Fig. 8(b)]. The latter island type is found at steps, where formerly straight Si steps are understood to evolve into less angular edges connected to the adjacent CaF_1 interface layer. Here, the interface layer etched the adatom, first, and second silicon layer relative to the top terrace, similar to the finding of type-II “islands” in pits on bare terraces. A kinetic phase diagram for the CaF_1 nucleation [72] identifies the conditions herein to support terrace nucleation over step nucleation, in agreement with the data presented in Fig. 3(a). However, the case of an “etch pit” has not been discussed before; furthermore, similar pits were never observed on a pristine Si surface in the course of our experiments.

Under the assumption that only F_2 or SiF_x (with $x \geq 1$) species desorb from the surface during CaF_1 interface growth

[22,61], it is instructive to quantify the involved species. The CaF_x film forms a (1×1) superstructure, thus 49 excess fluorine atoms are present within the Si (7×7) unit cell for a closed CaF_1 film. This number might be slightly reduced for submonolayer CaF_1 films due to the exclusive F-terminated island edges. Compared to the four excess silicon atoms for the formation of islands of type-I by only etching the adatom layer, the process generates excess fluorine which could be either present on the surface or which can desorb from the surface in the form of F_2 or SiF_x . Especially, our NC-AFM data confirm point-size defects within the islands of type-I (see Fig. 5), suggesting that these defects are formed by Si-F species. In contrast, etching down to the second Si layer—as suggested during the formation of islands of type-II—supplies 102 silicon atoms per 49 excess fluorine species. In this case, the process generates excess silicon, because a maximum silicon amount in the form of $(\text{Si}_1\text{F}_1)_{49}$ per (7×7) unit cell can desorb during the interface formation, leaving a minimum of 53 silicon atoms per (7×7) unit cell behind. Although the excess silicon could diffuse to islands of type-I with excess fluorine, we presume that the excess silicon within type-II islands causes the row structures shown in Fig. 6.

VI. CONCLUSIONS

By using a combination of high-resolution STM and NC-AFM we are able to reveal atomic-scale details and reaction processes of the $\text{CaF}_1/\text{Si}(111)$ interface grown at submonolayer coverages and at substrate temperatures between 550 and 600 °C. First, our data suggest the exclusive presence of F-terminated $(\bar{1}\bar{1}2)_{\text{CaF}_2}$ island step edges within the submonolayer CaF_1 interface, where especially the rough appearance in STM data of the apparent $(11\bar{2})_{\text{CaF}_2}$ step edges could be identified as small peaks formed by $(\bar{1}\bar{1}2)_{\text{CaF}_2}$ edges. The peak structure that appears rough in the STM imaging seems to

furthermore limit the growth along the $(1\bar{1}\bar{2})_{\text{CaF}_2}$ direction, ultimately leading to a triangular instead of a hexagonal shape of the CaF_1 islands.

Furthermore, we find two island types at submonolayer coverages, located either on bare terraces (type-I) or adjacent to Si step edges or within etch pits (type-II). The imaged island types suggest different reaction pathways where type-I (type-II) islands etch the adatom layer (adatom and first two silicon layers) and generate during this process excess F (Si) atoms, respectively. This interpretation is in agreement with atomic-scale details revealed by NC-AFM measurements: While the defects in type-I islands could be identified to be pointlike, thus excluding a large accumulation of excess silicon or fluorine material, a pronounced row structure is found within type-II islands, likely accommodating the excess silicon material.

Our paper further improves the understanding of the CaF_1 interface formation by clarifying several atomic-scale details of the CaF_1/Si system. A detailed understanding of the interface characteristics is most important for the fabrication of high-quality multilayer films.

ACKNOWLEDGMENTS

The research leading to these results has received funding from the People Programme (Marie Curie Actions) of the European Union's Seventh Framework Programme (FP7/2007-2013) under Research Executive Agency (REA) Grant No. 628439. We gratefully acknowledge Engineering and Physical Sciences Research Council Grant No. EP/K005138/1 for supporting use of the XPS in the Nanoscale and Microscale Research Centre (NMRC). We furthermore thank Adam Sweetman (The University of Nottingham) for valuable assistance with the STM and NC-AFM experiments and Karsten Küpper (Universität Osnabrück) for most helpful discussions.

-
- [1] G. Meyer, L. Gross, F. Mohn, and J. Repp, *CHIMIA International Journal for Chemistry* **66**, 10 (2012).
 - [2] J. Repp, G. Meyer, S. M. Stojković, A. Gourdon, and C. Joachim, *Phys. Rev. Lett.* **94**, 026803 (2005).
 - [3] J. Repp, G. Meyer, F. E. Olsson, and M. Persson, *Science* **305**, 493 (2004).
 - [4] W. Steurer, J. Repp, L. Gross, I. Scivetti, M. Persson, and G. Meyer, *Phys. Rev. Lett.* **114**, 036801 (2015).
 - [5] T. Leoni, O. Guillermet, H. Walch, V. Langlais, A. Scheuermann, J. Bonvoisin, and S. Gauthier, *Phys. Rev. Lett.* **106**, 216103 (2011).
 - [6] W. Steurer, S. Fatayer, L. Gross, and G. Meyer, *Nat. Commun.* **6**, 8353 (2015).
 - [7] C. Wäckerlin, F. Donati, A. Singha, R. Baltic, S. Rusponi, K. Diller, F. Patthey, M. Pivetta, Y. Lan, S. Klyatskaya, M. Ruben, H. Brune, and J. Dreiser, *Adv. Mater.* **28**, 5195 (2016).
 - [8] C. Bombis, F. Ample, L. Lafferentz, H. Yu, S. Hecht, C. Joachim, and L. Grill, *Angew. Chem., Int. Ed. Engl.* **48**, 9966 (2009).
 - [9] M. Watanabe, T. Suemasu, S. Muratake, and M. Asada, *Appl. Phys. Lett.* **62**, 300 (1993).
 - [10] C. R. Wang, B. H. Müller, and K. R. Hofmann, *Nanotechnology* **14**, 1192 (2003).
 - [11] C. R. Wang, M. Bierkandt, S. Paprotta, T. Wietler, and K. R. Hofmann, *Appl. Phys. Lett.* **86**, 033111 (2005).
 - [12] J.-Y. Chung, H.-D. Li, W.-H. Chang, T. C. Leung, and D.-S. Lin, *Phys. Rev. B* **83**, 085305 (2011).
 - [13] C.-Y. Chang, H.-D. Li, S.-F. Tsay, S.-H. Chang, and D.-S. Lin, *J. Phys. Chem. C* **116**, 11526 (2012).
 - [14] S. F. Tsay, J. Y. Chung, M. F. Hsieh, S. S. Ferng, C. T. Lou, and D. S. Lin, *Surf. Sci.* **603**, 419 (2009).
 - [15] I. Beinik, C. Barth, M. Hanbucken, and L. Masson, *Scientific Reports* **5**, 8223 (2015).
 - [16] M. Körner, F. Loske, M. Einax, A. Kühnle, M. Reichling, and P. Maass, *Phys. Rev. Lett.* **107**, 016101 (2011).
 - [17] F. Loske, M. Reichling, and A. Kühnle, *Jpn. J. Appl. Phys.* **50**, 08LB07 (2011).
 - [18] F. Loske, M. Reichling, and A. Kühnle, *Chem. Commun.* **47**, 10386 (2011).
 - [19] F. Loske, J. Lübke, J. Schütte, M. Reichling, and A. Kühnle, *Phys. Rev. B* **82**, 155428 (2010).
 - [20] F. J. Giessibl, *Appl. Phys. Lett.* **73**, 3956 (1998).
 - [21] K. Miura, K. Sugiura, R. Souda, T. Aizawa, C. Oshima, and Y. Ishizawa, *Jpn. J. Appl. Phys.* **30**, 809 (1991).

- [22] M. A. Olmstead, "Heteroepitaxy of disparate materials: From chemisorption to epitaxy in CaF₂/Si(111)", in *Thin Films: Heteroepitaxial Systems*, edited by W. K. Liu and M. B. Santos (World Scientific, Singapore, 1999), Vol. 15, Sec.5.
- [23] J. Wollschläger, "Resonant tunneling devices based on epitaxial insulator-semiconductor structures: Growth and characterisation of CaF₂ films on Si(111)", in *Recent Research Developments in Applied Physics*, edited by S. Pandalai (Transworld Research Network, Trivandrum, India, 2002), Vol. 5-II, pp. 621–695.
- [24] J. Wollschläger, *Appl. Phys. A* **75**, 155 (2002).
- [25] C. A. Lucas, D. Loretto, and G. C. L. Wong, *Phys. Rev. B* **50**, 14340 (1994).
- [26] M. A. Olmstead and R. D. Bringans, *J. Electron Spectrosc. Relat. Phenom.* **51**, 599 (1990).
- [27] N. S. Sokolov, J. C. Alvarez, S. V. Gastev, Y. V. Shusterman, I. Takahashi, Y. Itoh, J. Harada, and R. M. Overney, *J. Cryst. Growth* **169**, 40 (1996).
- [28] C. C. Cho, H. Y. Liu, B. E. Gnade, T. S. Kim, and Y. Nishioka, *J. Vac. Sci. Technol. A* **10**, 769 (1992).
- [29] J. Harada, I. Takahashi, Y. Itoh, N. S. Sokolov, N. L. Yakovlev, Y. Shusterman, and J. C. Alvarez, *J. Cryst. Growth* **163**, 31 (1996).
- [30] N. S. Sokolov, J. C. Alvarez, Y. V. Shusterman, N. L. Yakovlev, R. M. Overney, Y. Itoh, I. Takahashi, and J. Harada, *Appl. Surf. Sci.* **104-105**, 402 (1996).
- [31] U. O. Karlsson, F. J. Himpsel, J. F. Morar, D. Rieger, and J. A. Yarmoff, *J. Vac. Sci. Technol. B* **4**, 1117 (1986).
- [32] R. M. Tromp and M. C. Reuter, *Phys. Rev. Lett.* **61**, 1756 (1988).
- [33] D. Rieger, F. J. Himpsel, U. O. Karlsson, F. R. McFeely, J. F. Morar, and J. A. Yarmoff, *Phys. Rev. B* **34**, 7295 (1986).
- [34] C. R. Wang, B. H. Müller, E. Bugiel, and K. R. Hofmann, *J. Vac. Sci. Technol. A* **22**, 2182 (2004).
- [35] T. Asano and H. Ishiwara, *Appl. Phys. Lett.* **42**, 517 (1983).
- [36] M. A. Olmstead, R. I. G. Uhrberg, R. D. Bringans, and R. Z. Bachrach, *J. Vac. Sci. Technol. B* **4**, 1123 (1986).
- [37] T. Sumiya, *Appl. Surf. Sci.* **156**, 85 (2000).
- [38] M. A. Olmstead, R. I. G. Uhrberg, R. D. Bringans, and R. Z. Bachrach, *Phys. Rev. B* **35**, 7526 (1987).
- [39] D. Y. Petrovykh, K. N. Altmann, J. L. Lin, F. J. Himpsel, and F. M. Leibsle, *Surf. Sci.* **512**, 269 (2002).
- [40] A. A. Saranin, V. G. Lifshits, K. V. Ignatovich, H. Bethge, R. Kayser, H. Goldbach, A. Klust, J. Wollschläger, and M. Henzler, *Surf. Sci.* **448**, 87 (2000).
- [41] E. Rotenberg, J. D. Denlinger, M. Leskovic, U. Hessinger, and M. A. Olmstead, *Phys. Rev. B* **50**, 11052 (1994).
- [42] J. D. Denlinger, E. Rotenberg, U. Hessinger, M. Leskovic, and M. A. Olmstead, *Phys. Rev. B* **51**, 5352 (1995).
- [43] F. J. Himpsel, T. F. Heinz, A. B. McLean, and E. Palange, *Appl. Surf. Sci.* **41-42**, 346 (1989).
- [44] J. Zegenhagen and J. R. Patel, *Phys. Rev. B* **41**, 5315 (1990).
- [45] A. Klust, M. Bierkandt, J. Wollschläger, B. H. Müller, T. Schmidt, and J. Falta, *Phys. Rev. B* **65**, 193404 (2002).
- [46] N. S. Sokolov, T. Hirai, K. Kawasaki, S.-i. Ohmi, K. Tsutsui, S. Furukawa, I. Takahashi, Y. Itoh, and J. Harada, *Jpn. J. Appl. Phys.* **33**, 2395 (1994).
- [47] C. A. Lucas and D. Loretto, *Appl. Phys. Lett.* **60**, 2071 (1992).
- [48] G. C. L. Wong, D. Loretto, E. Rotenberg, M. A. Olmstead, and C. A. Lucas, *Phys. Rev. B* **48**, 5716 (1993).
- [49] C. A. Lucas, G. C. L. Wong, and D. Loretto, *Phys. Rev. Lett.* **70**, 1826 (1993).
- [50] Y. Itoh, I. Takahashi, A. Ichimiya, J. Harada, and N. S. Sokolov, *J. Cryst. Growth* **166**, 61 (1996).
- [51] K. G. Huang, J. Zegenhagen, J. M. Phillips, and J. R. Patel, *Physica B (Amsterdam)* **221**, 192 (1996).
- [52] P. Avouris and R. Wolkow, *Appl. Phys. Lett.* **55**, 1074 (1989).
- [53] J. Viernow, D. Y. Petrovykh, A. Kirakosian, J. L. Lin, F. K. Men, M. Henzler, and F. J. Himpsel, *Phys. Rev. B* **59**, 10356 (1999).
- [54] A. Klust, T. Ohta, A. A. Bostwick, E. Rotenberg, Q. Yu, F. S. Ohuchi, and M. A. Olmstead, *Phys. Rev. B* **72**, 205336 (2005).
- [55] T. Nakayama, M. Katayama, G. Selva, and M. Aono, *Phys. Rev. Lett.* **72**, 1718 (1994).
- [56] T. Nakayama and M. Aono, *Phys. Rev. B* **57**, 1855 (1998).
- [57] T. Sumiya, T. Miura, and S.-i. Tanaka, *Jpn. J. Appl. Phys.* **34**, L1383 (1995).
- [58] T. Sumiya, T. Miura, H. Fujinuma, and S.-i. Tanaka, *Jpn. J. Appl. Phys.* **35**, L1077 (1996).
- [59] T. Sumiya, T. Miura, and S. Tanaka, *Surf. Sci.* **357-358**, 896 (1996).
- [60] C. R. Wang, B. H. Müller, and K. R. Hofmann, *Thin Solid Films* **410**, 72 (2002).
- [61] C. R. Wang, B. H. Müller, and K. R. Hofmann, *Surf. Rev. Lett.* **10**, 605 (2003).
- [62] A. Klust, H. Pietsch, and J. Wollschläger, *Appl. Phys. Lett.* **73**, 1967 (1998).
- [63] A. Klust, Q. Yu, M. A. Olmstead, T. Ohta, F. S. Ohuchi, M. Bierkandt, C. Deiter, and J. Wollschläger, *Appl. Phys. Lett.* **88**, 063107 (2006).
- [64] A. Klust, T. Ohta, A. A. Bostwick, Q. M. Yu, F. S. Ohuchi, and M. A. Olmstead, *Phys. Rev. B* **69**, 035405 (2004).
- [65] A. S. Foster, C. Barth, A. L. Shluger, and M. Reichling, *Phys. Rev. Lett.* **86**, 2373 (2001).
- [66] C. Barth, A. S. Foster, M. Reichling, and A. L. Shluger, *J. Phys.: Condens. Matter* **13**, 2061 (2001).
- [67] R. Erlandsson, L. Olsson, and P. Martensson, *Phys. Rev. B* **54**, R8309 (1996).
- [68] Z. Majzik, M. Setvín, A. Bettac, A. Feltz, V. Cháb, and P. Jelínek, *Beilstein Journal of Nanotechnology* **3**, 249 (2012).
- [69] P. Rahe, J. Schütte, W. Schniederberend, M. Reichling, M. Abe, Y. Sugimoto, and A. Kühnle, *Rev. Sci. Instrum.* **82**, 063704 (2011).
- [70] D. Nečas and P. Klapetek, *Central Eur. J. Phys.* **10**, 181 (2012).
- [71] A preferential nucleation at phase boundaries of the (7 × 7) reconstruction as observed before [58] is also evident from our data.
- [72] J. Wollschläger, M. Bierkandt, and M. I. Larsson, *Appl. Surf. Sci.* **219**, 107 (2003).
- [73] J. Wollschläger, H. Pietsch, and A. Klust, *Appl. Surf. Sci.* **130-132**, 29 (1998).
- [74] H. H. Pieper, C. Barth, and M. Reichling, *Appl. Phys. Lett.* **101**, 051601 (2012).
- [75] T. G. Cooper and N. H. De Leeuw, *J. Mater. Chem.* **14**, 1927 (2004).
- [76] V. E. Puchin, A. V. Puchina, M. Huisinga, and M. Reichling, *J. Phys.: Condens. Matter* **13**, 2081 (2001).
- [77] A. V. Puchina, V. E. Puchin, M. Huisinga, R. Bennowitz, and M. Reichling, *Surf. Sci.* **402-404**, 687 (1998).
- [78] R. Wolkow and P. Avouris, *J. Microsc.* **152**, 167 (1988).
- [79] K. Kametani, K. Sudoh, and H. Iwasaki, *Jpn. J. Appl. Phys.* **41**, 250 (2002).

- [80] C. Barth, T. Hynninen, M. Bielecki, C. R. Henry, A. S. Foster, F. Esch, and U. Heiz, [New J. Phys.](#) **12**, 093024 (2010).
- [81] W. A. Hofer, A. S. Foster, and A. L. Shluger, [Rev. Mod. Phys.](#) **75**, 1287 (2003).
- [82] P. Hapala, G. Kichin, C. Wagner, F. S. Tautz, R. Temirov, and P. Jelínek, [Phys. Rev. B](#) **90**, 085421 (2014).
- [83] S. P. Jarvis, A. M. Sweetman, L. Kantorovich, E. McGlynn, and P. Moriarty, “Pauli’s principle in probe microscopy”, in *Advances in Atom and Single Molecule Machines*, Advances in Atom and Single Molecule Machines, edited by P. Moriarty and S. Gauthier (Springer-Verlag, New York, 2015), pp. 1–24.
- [84] K. Takayanagi, Y. Tanishiro, S. Takahashi, and M. Takahashi, [Surf. Sci.](#) **164**, 367 (1985).
- [85] A. A. Saranin, A. V. Zotov, S. V. Ryzhkov, D. A. Tsukanov, V. G. Lifshits, J. T. Ryu, O. Kubo, H. Tani, T. Harada, M. Katayama, and K. Oura, [Phys. Rev. B](#) **58**, 7059 (1998).